Scientific Research Publishing

Journal of Applied Mathematics and Physics, 2025, 13(1), 61-86
https://www.scirp.org/journal/jamp
ISSN Online: 2327-4379
ISSN Print: 2327-4352

Crystal Structures, Optical, Electrical and Magnetic Properties of $Ca_{0.9}Sr_{0.1}Mn_{1-x}Mo_xO_3$ Perovskites for the Applications of Multifunctional Devices

Sanjana Afrin[1,2], Tanvir Ahmed[1], Mithum Kumar Das[1], Mohammad Majibur Rahman[3], Mohammed Nazrul Islam Khan[4], Mohammad J. Miah[1*]

[1]Department of Physics, Comilla University, Cumilla, Bangladesh
[2]Department of EEE, Bangladesh University of Business and Technology, Dhaka, Bangladesh
[3]Department of Environmental Sciences, Jahangirnagar University, Dhaka, Bangladesh
[4]Materials Science Division, Bangladesh Atomic Energy Commission, Dhaka, Bangladesh
Email: *mmjulhash@yahoo.com

How to cite this paper: Afrin, S., Ahmed, T., Das, M.K., Rahman, M.M., Khan, M.N.I. and Miah, M.J. (2025) Crystal Structures, Optical, Electrical and Magnetic Properties of $Ca_{0.9}Sr_{0.1}Mn_{1-x}Mo_xO_3$ Perovskites for the Applications of Multifunctional Devices. *Journal of Applied Mathematics and Physics*, **13**, 61-86.
https://doi.org/10.4236/jamp.2025.131003

Received: October 19, 2024
Accepted: January 7, 2025
Published: January 10, 2025

Abstract

The standard solid-state reaction method was employed to synthesize the polycrystalline $Ca_{0.9}Sr_{0.1}Mn_{1-x}Mo_xO_3$ (CSMMO with $x = 0.00$, 0.02, 0.04, 0.06, and 0.08) ceramics and each composition was sintered at 1300˚C for 4 hours. The crystal structure, microstructure, optical properties, electrical properties, complex initial permeability, and DC magnetization of the prepared compositions were carried out. The compound exhibited perovskite structure with the transformation of phase from orthorhombic symmetry for $x = 0.00$ to $x = 0.04$ samples into a tetragonal symmetry for the samples $x = 0.06$ and $x = 0.08$. The lattice constant was found to be enhanced with the doping of Mo concentration. The mean grain size was estimated in the micrometer, with values from 1.3045 to 3.0124 μm. Energy band gap (E_g) was determined for each composition and the magnitudes of E_g were lying between 1.85 - 4.00 eV. The E_g values firstly decreased with the doping content up to 2% and, then, increased for 4% to 6% Mo contents, where it again very slightly decreased for 8% Mo content. The lowest value of E_g was obtained for the $x = 0.02$ composition. The FTIR spectra revealed the existence of a metal oxide band in each of the prepared samples and supported the formation of a single-phase compound of synthesized material without any impurity, as confirmed by the XRD analysis. The electrical properties, such as resistivity and AC conductivity, were collected using the Impedance analyzer at room temperature. The resistivity and AC conductivity increased with the addition of dopant concentration. The

frequency-dependent conductivity spectra showed three distinct regions. The complex initial permeability (μ') was found to be enhanced with the addition of Mo and the highest value was noticed the 6% Mo dopant sample. On the other hand, the lowest loss factor was obtained for the samples $x \geq 0.06$. The M-H hysteresis loops of various $Ca_{0.9}Sr_{0.1}Mn_{1-x}Mo_xO_3$ ceramics were measured both at room temperature (300 K) and low temperature (5 K). The values of saturation magnetization (M_s) and retentivity (M_r) were found to be larger at low temperatures than at room temperature (RT), although no saturation was obtained for any compositions. The highest saturation magnetization obtained at room temperature for the $x = 0.06$ sample was 0.8581 emu/g.

Keywords

Perovskite, Optical Band Gap, Conductivity, Permeability, DC Magnetization

1. Introduction

Calcium manganite ($CaMnO_3$) is a manganese-based compound having ABO_3-type perovskite structure. There are numerous uses for the ABO_3-type perovskite in engineering and technology [1]. Physical attributes of perovskites can be altered by small changes in the percentage of A and B cations or the procedure of synthesis process [2]. Other properties, such as ferroelectricity, dielectricity, optical, and magnetic properties can be modified by doping with transition metals, alkaline earth, alkaline, and rare earth metals [1]. Perovskites are of two types: halide perovskite and oxide perovskite. Among the oxide perovskite, $CaMnO_3$ is a typical perovskite material which displays unique characteristics in magnetic, electric, and optical properties, and has been a research hot spot. It is possible to successfully control the electromagnetic characteristics of $CaMnO_3$ by varying the kind and concentration of doping ions. $CaMnO_3$ exhibits G-type antiferromagnetism (AFM) together with modest ferromagnetic characteristics in its ground state [3]-[6]. Supelano *et al.* [7] reported that $CaMnO_3$ have orthorhombic perovskite structure when Mo is added in B-site ($CaMn_{1-x}Mo_xO_3$) and the phase was stable up to 12% molybdenum concentrations. They also reported that the $CaMn_{1-x}Mo_xO_3$ have antiferromagnetic-like behavior. Continuing, it was appreciated as a ferromagnetic-like behavior. Doping of Mo in Mn-site results in the transition of antiferromagnetic property and, thus, a modification in magnetic properties is noticed. The complex permittivity and permeability for Ni doped $CaMnO_3$was investigated by Liu *et al.* [8]. The complex permittivity had dramatically changed with increasing Ni-doping, first increasing and then decreasing. Single-phase perovskite-structure for $La_{0.1}Ca_{0.9}MnO_3$ powders were prepared successfully by Jiang *et al.* [9] and they reported that the dielectric loss ($\tan\delta_e$) and magnetic loss ($\tan\delta_m$) decreases with La concentration. The doping La^{3+} atoms at A-site of ABO_3 perovskite oxide affect the dielectric loss more than the magnetic loss. Very recently Liu *et al.* [10] synthesized $Ca_{1-x}Sr_xMnO_3$ powders *via* a solid-state reaction

technique. The complex permittivity of the $CaMnO_3$ was greatly increased by Sr-doping. The positions of the element Sr and Ca in periodic table are in the same group, but there is a difference in ionic radius. The volume of unit cell is expanded when Ca is substituted by Sr in $CaMnO_3$ because of mismatch in ionic radius and, thus, improved dielectric properties were found. But to the best of our knowledge, the reports on the properties of Sr^{2+} and Mo^{6+} doped simultaneously in $CaMnO_3$ ceramics ($Ca_{0.9}Sr_{0.1}Mn_{1-x}Mo_xO_3$) were not investigated adequately. Considering the above results, the synthesis of $Ca_{0.9}Sr_{0.1}Mn_{1-x}Mo_xO_3$ ceramics was selected in the present work. Herein, the influence of Mo addition in the crystal structure, microstructure, optical properties, electrical properties, complex initial permeability, and DC magnetization of the synthesized compositions were described in great detail.

2. Experimental Methodology

2.1. Sample Preparation

$Ca_{0.9}Sr_{0.1}Mn_{1-x}Mo_xO_3$ [CSMMO with x = 0.00, 0.02, 0.04, 0.06, and 0.08] ceramics were prepared utilizing a typical solid-state reaction process using the raw materials $CaCO_3$ (99.999%), $SrCO_3$ (99.99%), MoO_3 (99%), and MnO_2 (99%). To study the effects of changes in perovskite characteristics caused by dopants, a very small amount of Mo was doped rather than a higher-order dopant level. In an agate mortar, powders of the raw materials were combined according to stochiometric calculation and grounded with acetone. Each composition was milled for 6 hours to ensure a homogenous blend. After that, each composition was calcined at 900˚C for 3 hours in the furnace. The calcined powders were ground again for roughly 4 hours after calcination. By combining polyvinyl alcohol (PVA) with the weighted sample, disc- and toroid-shaped samples were created using a hydraulic press at 5 tons of uniaxial pressure. Finally, the green samples had been sintered at 1300˚C for 4 hours.

2.2. Characterization

X-ray diffractometer (Rigaku Smart Lab, Japan) was used to determine the material's crystal structure. The specimens were subjected to Cu-K_α radiation with a primary beam of 40 kV and 30 mA at a wavelength of λ = 1.54056 Å. The lattice parameters for orthorhombic structure were calculated using the formula:

$$\frac{1}{d_{hkl}^2} = \frac{h^2}{a^2} + \frac{k^2}{b^2} + \frac{l^2}{c^2} \tag{1}$$

and for the tetragonal structure, the following formula was used:

$$\frac{1}{d_{hkl}^2} = \frac{h^2 + k^2}{a^2} + \frac{l^2}{c^2} \tag{2}$$

where d_{hkl} is the d spacing between the crystal planes, and (h, k, l) are the Miller indices, and a, b, c are the values of the lattice parameter.

The JOEL 7500 scanning electron microscope was utilized to obtain the

microstructural photographs of the samples to get a better understanding of grain structures. The Jusco FT-IR 6300 spectrophotometer was used to measure the Fourier Transformation Infrared Spectra (FTIR) at room temperature. Hitachi U-2900 UV–Vis Double Beam Spectrophotometer was used for measuring the UV–visible absorption spectra. Electrical properties, such as resistivity, ac conductivity, were collected by the Wayne Kerr Impedance Analyzer (WAYNE KERR 6500B). The samples' ac conductivity (ac) was estimated using the following formula:

$$\sigma_{ac} = \omega\varepsilon_o\varepsilon' \tan\delta_E \tag{3}$$

where ω is the angular frequency.

The Wayne Kerr Impedance Analyzer (WAYNE KERR 6500B) was also utilized to determine the magnetic properties, such as permeability; at room temperature over the frequency range of 1 kHz to 100 MHz. The real part of the complex primary permeability (μ_i') was calculated using the following formula:

$$\mu_i' = \frac{L_s}{L_o} \tag{4}$$

$$\text{and} \quad \mu_i'' = \mu_i' \tan\delta \tag{5}$$

where L_s is the sample core's self-inductance and $L_o = \mu_o N^2 S/d$ is determined geometrically. L_o is the inductance of the winding coil without the sample core, N is the number of turns of the coil ($N = 4$), and S is the area of the toroidal sample's cross-section.

The M-H hysteresis loops have been collected at room temperature and also at low temperature (5K) by using the Physical Properties Measurement System (PPMS), Quantum Design Dyna Cool to reveal the magnetic properties of the resulting materials.

3. Results and Discussion

3.1. Structural Analysis

XRD is a very important tool to determine the structural parameters of any materials. **Figure 1** shows the XRD patterns of $Ca_{0.9}Sr_{0.1}Mn_{1-x}Mo_xO_3$ (CSMMO) ceramics taken at room temperature (RT) using CuK_α (λ = 1.5406 Å) radiation. The diffraction patterns have been collected in the 2θ range of 20 to 80˚ for all bulk materials. All XRD peaks have been assigned using the JCPDS card No. #50-1746 [11] [12], which corresponds to orthorhombic symmetry. With increasing doping content, the orthorhombic crystal structure of the samples is transformed into a tetragonal symmetry. The orthorhombic phase of these manganates' changes into the tetragonal crystal structure when heated at high temperatures [13]. The phase transition from orthorhombic to tetragonal sintered at 1300˚C coincides with earlier research findings [14]. The substitution of Mo at the Mn site in CSMMO causes a structural transformation from an orthorhombic to a tetragonal crystal system, indicating that manganates have mixed valences of Mn. When there is an oxygen deficiency, the Mn^{4+} valence state decreases to Mn^{3+} for charge valence in

the lattice. New peaks are shown in the X-ray diffraction pattern (at about a 33-degree angle) for x > 0.04 samples, which indicates the transformation of crystal symmetry and it might be responsible for the lattice distortion due to the Jahn teller ion Mn^{3+} [15].

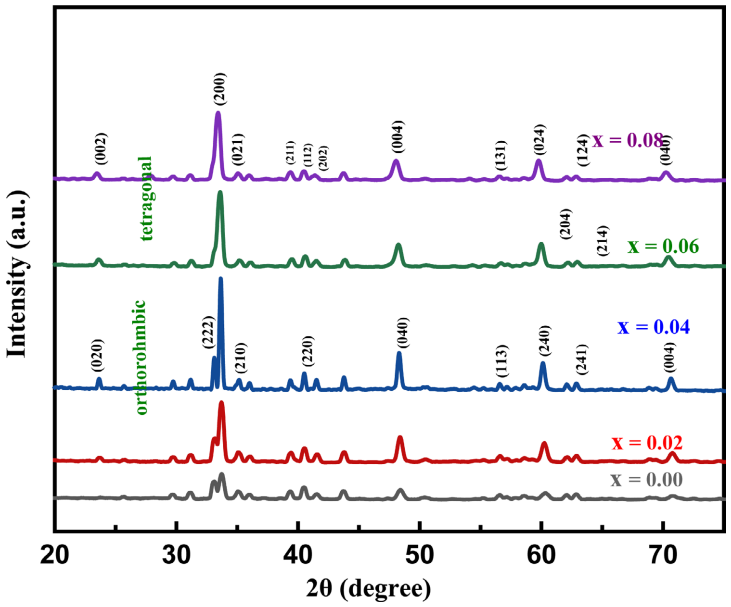

Figure 1. X-ray diffraction patterns of different CSMMO ceramics.

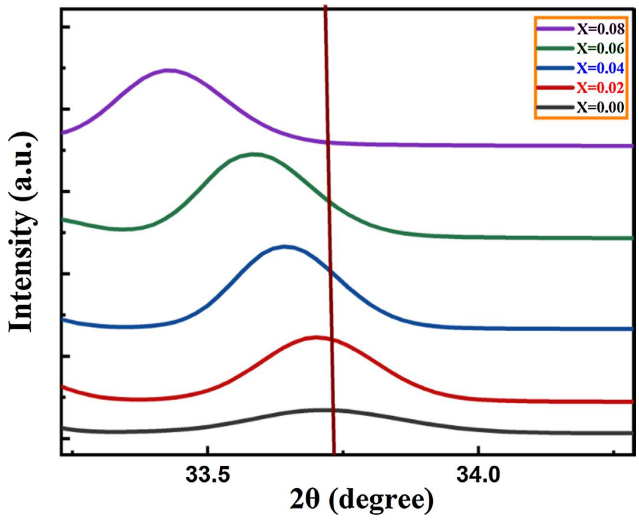

Figure 2. The enlarged view of prominent peaks (200) of various $Ca_{0.9}Sr_{0.1}Mn_{1-x}Mo_xO_3$ ceramics.

Figure 2 shows the enlarged view of (200) peaks and it confirms the shifting of peaks to the lower angle side. The phenomenon of shifting to lower angles with increasing Mo concentrations can be attributed to the size mismatch effect of Mn^{4+} (0.53 Å) and Mo^{6+} (0.59 Å) [16]. The shifting of the peaks is not only responsible due to the substitution of Mn^{4+} ions for Mo^{6+} ions, but, also, due to the conversion of Mn^{4+} by Mn^{3+} [17]. Since the samples have been synthesized at a

relatively high temperature (1300˚C), such as in the present case, the possibility of oxygen loss cannot be ruled out given by the following equation:

$$O_0 \rightarrow \frac{1}{2}O_2(g) + V_{\ddot{O}} + 2e' \tag{6}$$

where the defects are written in terms of Kroger-Vink notation of defect. The presence of an electron in Equation (6) may reduce the valence state of Mn^{3+}, given by the following equation:

$$Mn^{4+} + e' \rightarrow Mn^{3+} \tag{7}$$

The ionic radius of Mn^{3+} (0.64 Å) is higher than Mn^{4+} (0.53 Å), which increases the volume of the unit cell. Therefore, a higher value of interplanar spacing/lattice parameters gives a lower Bragg angle and *vice versa* [16]. The Mn^{3+} ions are increased according to the formula:

$$CaMn_{1-3y}^{4+}Mn_{2y}^{3+}Mo_y^{6+}O_3 \tag{8}$$

Therefore, the effective valency of Mn is equal to $\vartheta_{Mn} = (4-6y)/(1-y)$, provided there is no oxygen deficiency [18]. A decreased Mn effective valency with doping, as shown in Equation (7), indicates the further generation of Mn^{3+}, which causes orthorhombic distortion of MnO_6 octahedra in $x = 0.00$ to $x = 0.04$ sample, and then transform into tetragonal structure in $x = 0.06$ and $x = 0.08$ sample.

The lattice parameters and cell volume have been calculated as a function of doping atomic radii in structure optimization calculations and are shown in **Table 1**. It can be observed that with increasing Mo^{6+} content, the lattice parameters "*a*", "*b*" and "*c*" undergo an increase, with the overall increase in cell volume. This can be attributed to the substitution of Mn^{4+} ($r_{Mn^{4+}} = 0.53$ Å) with a larger ion Mo^{6+} ($r_{Sr^{2+}} = 0.59$ Å) [19]. The unit cell volume of the orthorhombic crystal can be derived from the formula, $V = a \times b \times c$ and for tetragonal, the formula is $V = a^2 \times c$. A gradual rise in the lattice parameters and unit cell volume correlates with the increased concentration of big charge-compensating Mn^{3+} cations resulting from Mo doping. In accordance with the rise in crystal symmetry, the Mn-O-Mn bond angle has consistently approached 180˚ with respect to *x*, which is consistent with earlier work and it is evident that *Sr* substitution enlarges the Mn-O-Mn bond angle, assisting one electron transfer of the extra electrons generated by Mo substitution [14]. The substitution of Mo in the B-site promotes a mixed valence state for Mn. Therefore, the substitution of *x* mole% of Mo to the B-site generates 2*x* mole% of Mn. This established the effect of Mo substitution by demonstrating that the Fermi level is dominated by Mn^{3+} and O^{2-} states, which are only present when Mo replacement is performed on Mn-sites. The Mo substitution only has the effect of raising the concentration of electronic carriers, which in turn modifies the material's electrical characteristics [20].

In addition, all the materials doped with Mo have a larger volume than that of intrinsic $CaMnO_3$. The values of *a* and *c* have increased with Mo substitution on the B-site, and it is more significant in the *a*-*c* plane. As a consequence, the orthorhombicity factor (*a*/*c*) has decreased strongly where the *c*/*a* value has increased,

from which it can be said that the tetragonality is increased with the increase in dopant contents [21], which is listed in **Table 1**.

Table 1. Lattice parameters, crystal structure, cell volume, *c*/*a* ratio, *a*/*c* ratio, and tolerance factor of various CSMMO ceramics.

Content (x)	Crystal structure	Lattice parameter in (nm)			V in $(nm)^3$	c/a	a/c	t
		a	b	c				
0.00	Orthorhombic	0.539	0.748	0.527	0.213	0.976	1.025	0.8296
0.02	Orthorhombic	0.531	0.751	0.531	0.212	0.999	1.000	0.8294
0.04	Orthorhombic	0.532	0.752	0.533	0.214	1.002	0.998	0.8292
0.06	Tetragonal	0.533	…….	0.753	0.215	1.414	0.707	0.8290
0.08	Tetragonal	0.536	…….	0.757	0.217	1.417	0.706	0.8288

3.2. Tolerance Factor

The chemical flexibility of perovskite materials and the potential substitution of A and B-site metal ions may result in cell deformation. The distortion is characterized by the Goldschmidt tolerance factor "*t*", which has the following definition [22] and leads to structural stability:

$$t = \frac{R_A + R_O}{\sqrt{2}\left(R_B + R_O\right)} \tag{9}$$

where R_A, R_B, and R_O represent the ionic radius of the A-site cation, B-site cation, and O-anion. According to the previous research [23], the perovskite structure will be cubic for $0.90 < t < 1.00$ and orthorhombic for $0.75 < t < 0.90$. The $CaMnO_3$ has a t of slightly less than 1.00, and for CSMMO, slightly greater than 0.82. In the case of $Ca_{0.9}Sr_{0.1}Mn_{1-x}Mo_xO_3$ ceramics, the above equation can be written as,

$$t = \frac{0.9R_{Ca^{2+}} + 0.1R_{Sr^{2+}} + R_{O^{2-}}}{\sqrt{2}\left[\left(1-x\right)R_{Mn^{4+}} + xR_{Mo^{6+}} + R_{O^{2-}}\right]} \tag{10}$$

where $R_{Ca^{2+}}$, $R_{Sr^{2+}}$, $R_{Mn^{4+}}$, $R_{Mo^{6+}}$, and $R_{O^{2-}}$ are the ionic radii of Ca, Sr, Mn, Mo, and O, respectively, and their respective values are 1.34, 1.44, 0.53, 0.59, and 1.40 Å [24].

The tolerance factor "*t*" is calculated for all samples and is listed in **Table 1**. The variation of "*t*" with Mo concentration is plotted in **Figure 3**. It was found that the tolerance factor deceased with increasing Mo concentration, and the value of "*t*" varies from 0.8296 to 0.8288. The tolerance factor decreased due to the increased radius of the dopant metal cations. This can lead to distortion and, eventually, decomposition of the perovskite structure. The values obtained for "*t*" agree well with the values observed due to Mo^{6+}doping at the Mn sites with their ionic radii [25].

3.3. Crystallite Size, Macrostrain, and Dislocation Density Study

The average crystallite size for CSMMO ceramics with varying dopant contents

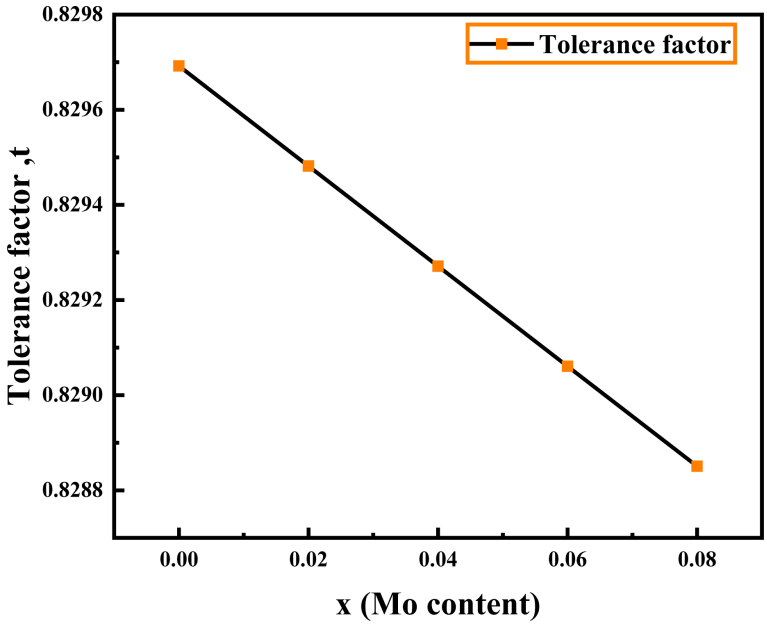

Figure 3. Variation of t with Mo concentrations in CSMMO ceramics.

has been calculated using the Scherrer equation below:

$$D = \frac{k\lambda}{\beta \cos\theta} \tag{11}$$

where D is the average crystallite size (nm), θ is the angle of diffraction, k is Scherrer's constant ($k = 0.94$), λ is the X-ray wavelength (0.15405 nm), and β is the full width at half maximum (FWHM) of the diffraction peak in radian[26].

To determine the accurate value of crystallite size, as well as micro-strain for the prepared samples, the Williamson-Hall (W-H) plot was considered. According to the W-H plot, the FWHM of the XRD peak is related to the average crystallite size (D) and average micro-strain (ε) is determined by a mathematical equation given as follows [26]:

$$\beta \cos\theta = \frac{0.9\lambda}{D} + 4\varepsilon \sin\theta \tag{12}$$

The value of average dislocation density, δ, is also calculated using the relationship [27]:

$$\delta = \frac{1}{D^2} \tag{13}$$

The values of D, ε, and δ have been calculated for all samples and the values are listed in **Table 2**. It can be observed that the micro-strain (ε) is increased up to 2% and, then, suddenly decreased up to 4%, and, then, it again increased up to 8% Mo doping. This may be because, as the dopant increases, the system becomes less crystallized, and, therefore, the ε in the system becomes higher. Equation (12) shows that the D is inversely proportional to the FWHM of the XRD peak, so the FWHM becomes higher, and therefore, corresponding D is lower, and similarly, ε is higher [26]. **Table 2** also shows the variation of δ with Mo doping. It is also

noticed that the value of δ is enhanced with the doping content. Eq. 13 reveals that the square of δ is inversely proportional with D. So, as D is decreased with the dopant, the value of δ is increased [27].

The average value of crystallite size (D) is found to be from 31.6418 to 35.6372 nm (Table 2). The D decreased with the increase in Mo concentration up to 2% Mo, and further doping increases its value upto 4% and, then, decreases again upto 8% due to the ionic size mismatch of Ca^{2+} (1.34 Å) and Sr^{2+} (1.44 Å), and similarly for Mn^{4+} (0.53 Å) and Mo^{6+} (0.59 Å) ions or due to strain-induced on doping process [28] [29].

Table 2. The values of D, ε, and δ of CSMMO ceramics.

Content (x)	Crystallite size (D) (in nm)	Microstrain (ε)	Dislocation density (δ) (in nm^{-2})	Average grain size in (μm)
0.00	34.28305	0.00302	0.001252	1.3045
0.02	33.06101	0.003091	0.001271	1.4525
0.04	35.6372	0.002971	0.00125	1.7520
0.06	34.28305	0.003214	0.001308	2.3671
0.08	31.6418	0.003244	0.001317	3.0124

3.4. Microstructural Study

The microstructure of the prepared samples is analyzed by FESEM. The typical FESEM images with 5000× magnification of various $Ca_{0.9}Sr_{0.1}Mn_{1-x}Mo_xO_3$ (x = 0.0, 0.02, 0.04, 0.06, and 0.08) solid solution sintered at 1300˚C for 4 hours are shown in Figure 4. Figure 4(a) depicts the microstructure of undoped $Ca_{0.9}Sr_{0.1}MnO_3$ ceramics and Figures 4(b)-(e) shows the images of Mo-doped various compositions. The FESEM images reveal that all the samples exhibit a compact arrangement of amalgamated, irregular, and inhomogeneous grains with spherical shape. Reasons for the agglomeration of the particles might be due to the presence of magnetic interactions among the particles. Roughness of surface and a very less amount of porosity is also occurring between the crystal grains, affecting the material density.

The grain size of the compositions has been estimated using the ImageJ software. The histogram of grain size distribution of various compositions is shown in Figures 5(a)-(e), and the values of average grain size are listed in Table 2. The observed grain sizes of the samples are 1.3, 1.45, 1.75, 2.36, and 3.01μm for x = 0.00, 0.02, 0.04, 0.06, and 0.08 samples, respectively.

The grain size is found to be increased with the increase in Mo contents in the compositions which suggests that Mo^{6+} might enhance the grain growth. Due to this grain growth, the average grain size goes higher and distribution of grains becomes wide. This can be explained by the tendency of the manganese to form more stable oxides than molybdenum [30]. As seen, the grain size increases with the molybdenum content, and it is further recommended that for Mo^{+} ions, less

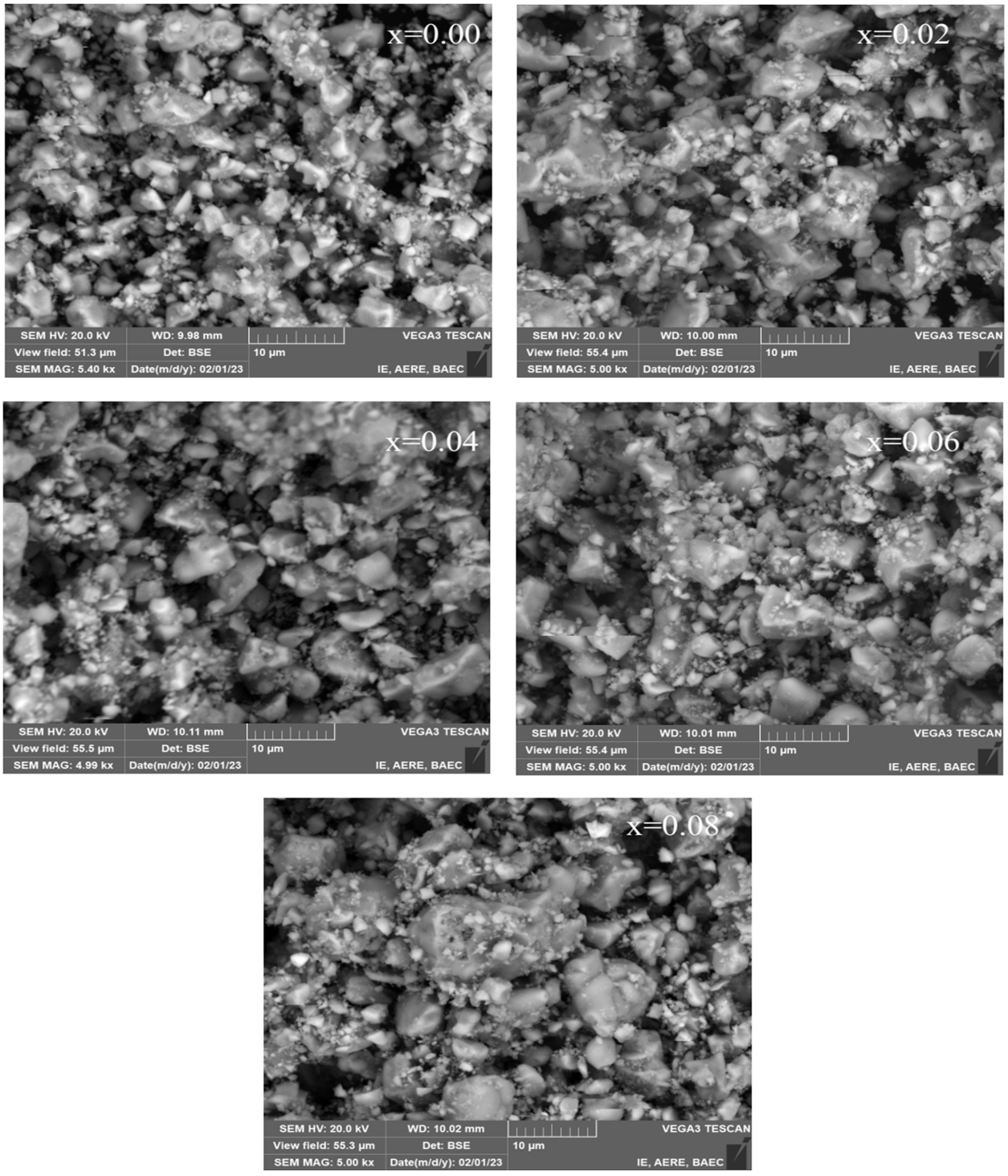

Figure 4. FESEM images of various CSMMO ceramics.

energy is required to penetrate into the lattice for the formation of the Mo^{+6}-O^{2-} bond, which is small as compared to the Mn^{3+}-O^{2-} bond [12]. Consequently, bigger size grains have observed with increasing Mo^{+} doping in the prepared $Ca_{0.9}Sr_{0.1}Mn_{1-x}Mo_xO_3$ ceramics. The result is in good agreement with the result of recent study on Mo doped $CaMnO_3$ solid solution system [7].

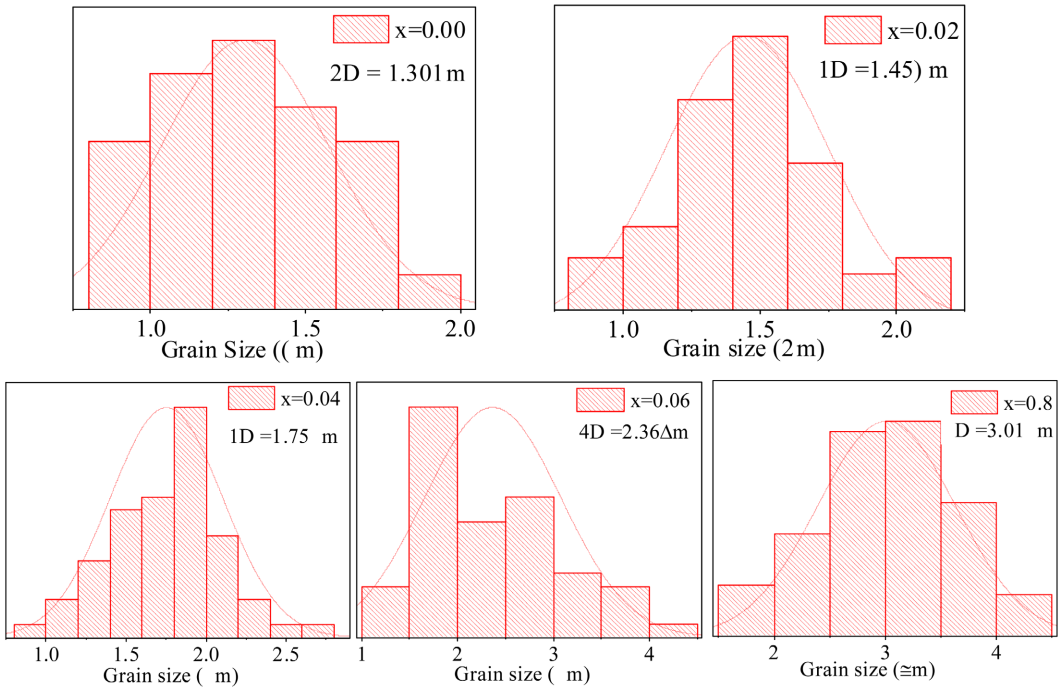

Figure 5. Histograms for grain distribution of CSMMO ceramics.

3.5. Ultraviolet-Visible Spectroscopy

The optical properties of Mo-doped $Ca_{0.9}Sr_{0.1}MnO_3$ ceramics have been analyzed by the Ultraviolet-visible (UV-vis) spectral studies and Fourier Transform Infrared Spectroscopy (FTIR). The UV-vis spectral studies give information on the energy gap and the transitions that form the optical absorption edge. Moreover, the optical properties of FTIR can be used to reveal the phase separation in the electron subsystem. The optical properties of $Ca_{0.9}Sr_{0.1}Mn_{1-x}Mo_xO_3$ ($x \leq 0.08$) polycrystals have been studied in the visible region. The purpose of this work is to study the effect of electron doping of $CaMnO_{3-}$ based manganite's, in which, Mn^{4+} ions are substituted by Mo^{6+} ions, on the band structure. The optical properties in the inter-band absorption have been investigated at room temperature (T = 300 K), *i.e.*, in the paramagnetic phase. The majority of inorganic compounds, organic compounds, and some functional groups have been noticed transparent in the UV-visible area. In order to investigate the optical absorbance spectra and their corresponding optical band gaps, the absorption spectrum of the specimens was collected by ultrasonicating a small quantity of the specimen in distilled water. The distilled water was employed as the reference point in this instance. The absorbance is located within 200 - 800 nm, which has been determined from the absorption spectrum (**Figure 6**). The energy of band gaps has been calculated for CSMMO ceramics using the Tauc plot method.

The Tauc equation is:

$$(\alpha h\nu)^{\gamma} = A(h\nu - E_g) \tag{14}$$

where α is the absorption coefficient, h is the Planck's constant, ν is the Photon's frequency, A is the proportionality constant that corresponds to the inter-band transition probability, and E_g is the band gap energy.

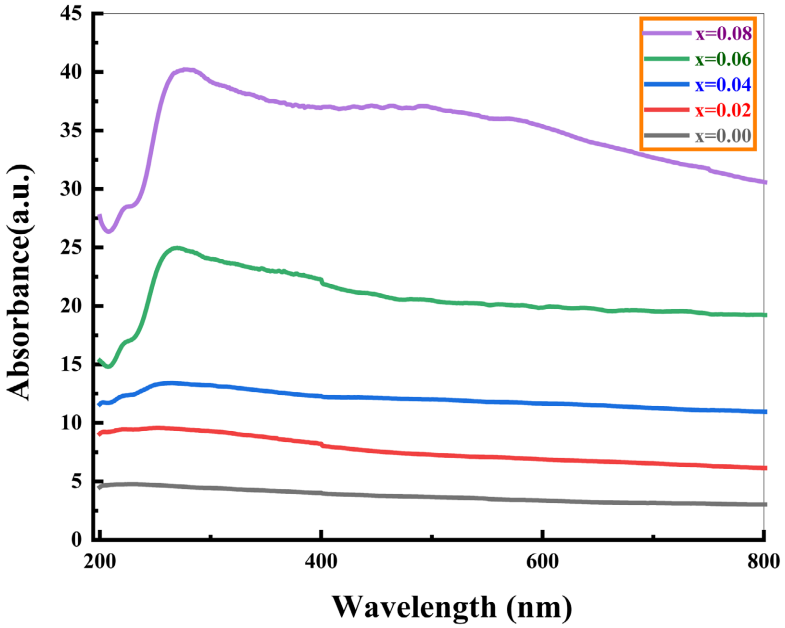

Figure 6. UV-vis absorption spectra of CSMMO ceramics.

The exponent γ is referred to as an index parameter that characterizes the kind of transitions occurring in electronic bands. Based on the type of transition, there are four potential values, such as 1/2, 1, 3/2, and 2 which correspond to allow indirect, forbidden indirect, forbidden direct, and allowed direct transitions, respectively [16]. Here,

$$\text{Absorption Coefficient, } \alpha = \frac{\text{absorbance}}{\text{thickness}} \tag{15}$$

According to the Beer-Lambert's law and from the absorption spectrum, α has been calculated.

The energy has been calculated from the following equation:

$$\text{Energy} = h\nu = hc/\lambda \tag{16}$$

The onset absorption edge of each sample has been determined by extrapolating the absorption edge on the wavelength axis. The absorption edges have been found at 228, 253, 271, 264, and 275nm for x = 0.00, 0.02, 0.04, 0.06, and 0.08, respectively, owing to its charge transfer intermolecular $\pi \rightarrow \pi^*$ transitions taking place in CMO ceramics [31].

To determine the optical band gaps of various samples of CSMMO ceramics, the plots of $(\alpha h\nu)^{1/2}$ *vs.* energy are used as shown in **Figure 7**. It is evident that the optical band gaps of CSMMO ceramics are indirect band gaps which are 2.05, 1.85, 3.00, 4.06, and 4.00 eV for x = 0.00, 0.02, 0.04, 0.06, and 0.08, respectively. The obtained values are presented in **Table 3**. The optical band gap firstly

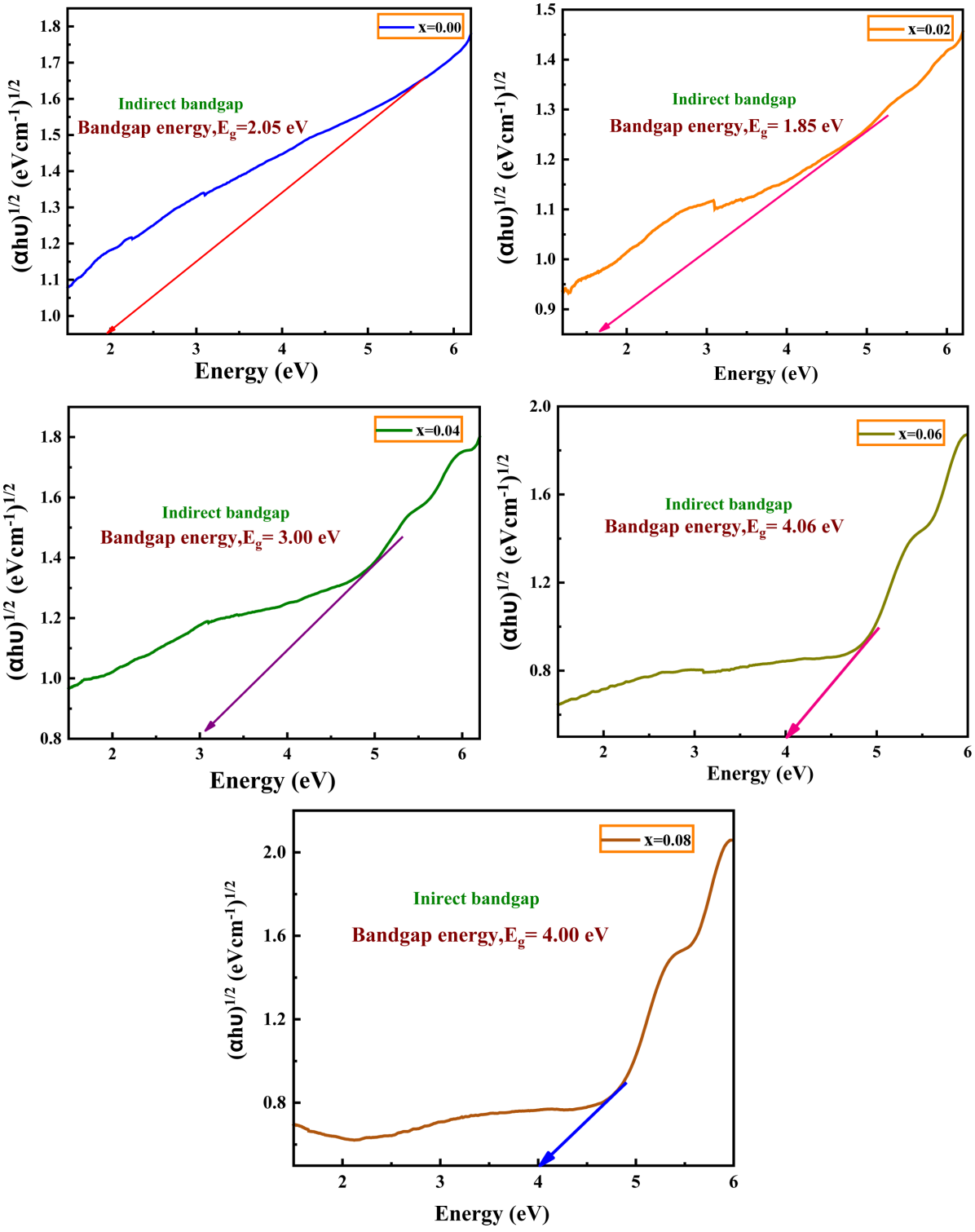

Figure 7. The Tauc plot for the indirect band gap of CSMMO ceramics.

decreased with doping content up to 2% and, then, increased with 4% and 6% Mo contents, where it, again, slightly decreased for 8% Mo content. The variation of E_g with Mo content follows the variation of average grain size with the addition of Mo, as shown in Table 2. It is a well-known quantum mechanical phenomenon

Table 3. Optical band gap of various CSMMO ceramics.

contents (x)	Band gap
0.00	2.05
0.02	1.85
0.04	3.00
0.06	4.06
0.08	4.00

that, with increasing particle size, the band gap of the materials has been found to increase [32]. In the previous study of the optical properties of $CaMnO_{3-\delta}$ single crystals, the fundamental absorption edge corresponds to $E_g = 1.55$ eV and is determined by indirect transitions; the intense inter-band absorption bands at 2.2 and 3.1 eV are explained by the O(2p) →$Mn(e_g)\uparrow$ and O(2p) → $Mn(t_{2g})\downarrow$ transitions; and the increase in absorption above 4.5 eV is related to the O(2p) $Mn(e_g)\downarrow$ transitions. In the manganese oxides perovskite, Mn-e_g and Mn-t_{2g} orbitals form r and p bonding with O-2p orbitals, respectively [33].

The energy band gap values exhibit a non-linear trend with the doping concentration. The samples containing low amount of Mo exhibit narrow band gap, whereas higher amount Mo doped samples show wide band gap. Hence, the prepared samples can be used for different purposes. Based on the optical studies, at the initial stage for $x = 0.02$, the value of E_g is found to reduce with the increase in Mo content and this might be attributed to the difference in the dopant's electronic structure. The $x = 0.02$ sample can be used as a potential candidate for photocatalytic and photovoltaic applications, in the regime of Infrared detector and infrared vision. The $x = 0.04$ sample can be applied as a potential candidate in radiation filter, UV-detector, and UV-sensor, and $x = 0.06$ and 0.08 samples can be used in supercapacitor applications [16] [31].

3.6. Fourier Transform Infrared (FTIR) Spectroscopy

The FTIR spectroscopy was used to determine the purity and nature of calcium manganese oxide metals obtained *via* the solid-state reaction method, as well as to examine the structural behavior and detect the chemical bands. It is a very reliable tool for manganite systems, which gives information about different functional groups existing in a compound. The functional groups that are present in the studied compound are metal-oxygen (M-O) bands and metal-oxygen-metal (M-O-M) bands. Functional groups are important in materials performance because they are the portion of a molecule that is capable of characteristic reactions. **Figure 8** depicts the FTIR spectra of various $Ca_{0.9}Sr_{0.1}Mn_{1-x}Mo_xO_3$ceramics. There are several peaks present in the study range of 1000 cm^{-1} to 350 cm^{-1}. The undoped samples have absorption peaks at 661, 583, 402, 369, and 360 cm^{-1}. The FTIR spectrum further confirms that the product is single phase. The bands at 661 and 583 cm^{-1} can be assigned to the M–O (metal-oxygen bands)stretching bonds and O–

M–O deformation modes of tetrahedral A- and octahedral B-sites of $CaMnO_3$. While the bending mode around 402 cm^{-1} is due to changes in the Mn-O-Mn (metal-oxygen-metal bands) bond angle [22] [31]-[33]. It has also been noticed that the FTIR spectra for varying concentrations of Mo have been assigned to the Mn-O-Mn deformation and Mn-O stretching modes of CSMMO. It can be seen from the figure that, with increasing the doping level of Mo, the absorption peaks have been shifted toward a lower wave number, where ν_1 for $x = 0.00$ was 661 cm^{-1}, which was shifted to 660 cm^{-1}. Similarly, ν_2 at $x = 0.00$ was 583 cm^{-1} and it was shifted to 577 cm^{-1}, ν_3 for $x = 0.00$ was 402 cm^{-1}, which was shifted to 395 cm^{-1}. This also confirms the formation of a single-phase compound of synthesized material without any impurity, as confirmed previously by the XRD analysis. The overall findings follow the XRD results. The changes mentioned above for doped samples are due to the sensitivity of vibration to octahedral distortion, and the variation of the bond length depends only on the level of doping of the atom and the nature of the atom [16] [34]. The FTIR spectrum was also taken for the doped samples and the peaks observed at 660, 577, 395, 364, and 355 cm^{-1}.

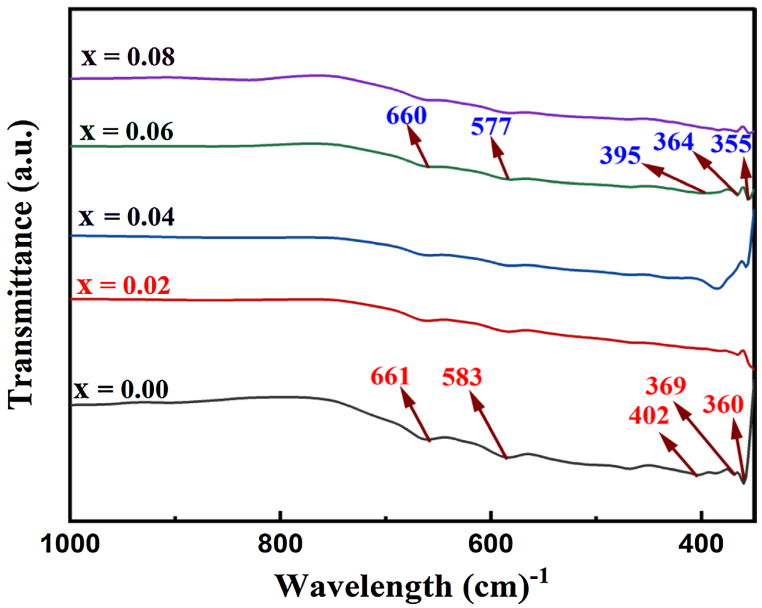

Figure 8. FTIR spectra of various CSMMO ceramics.

3.7. Resistivity Study

The resistivity (ρ) is an intrinsic property of electric materials and it is essential to know about the resistivity for device applications. **Figure 9** shows the variation of ρ with frequency. It is observed that ρ decreases significantly with increasing frequency and is invariable at high frequencies. The consistent behavior of ρ suggests the possible release of interfacial polarization or buildup at the interface of homogeneous phases when subjected to an electric field [35]. It can also be seen that the ρ increases with doping concentration. This enhancement in ρ elevates the eddy

current loss and to a lesser degree, the multiple scattering loss and resonance loss may also rise. Related research showed the similar behavior of ρ for B-site doped $CaMnO_3$ [36]. The $x = 0.08$ sample comprises the maximum ρ. This results from the generation of supplementary charge carriers caused by the presence of Mn^{3+} within the Mn^{4+} matrix. Besides, the distortion of the lattice and other crystal defects caused by Mo-doping produce more dipoles in the ac field [37]. For ceramic samples, ρ is significantly influenced by grain size, grain boundaries, density, porosity, oxygen concentration, and other factors, which may vary considerably among samples produced by different synthesis processes. According to the valence equilibrium, the substitution of Mo^{6+} in Mn^{3+} sites generates a substantial quantity of charge carriers, which can reduce ρ. Consequently, a rise in dopant concentration is expected to result in a steady reduction of ρ in this system. In previous research, it was demonstrated that larger concentrations of Mn^{3+} result in a decrease in resistivity. However, this interpretation is not clear since the behavior is highly impacted by the configuration of oxygen vacancies (V_o), which are intrinsic defects that cannot be avoided in perovskite materials [7] [38]. The presence of Mo doping defects is demonstrated to elevate the concentration of Mn^{3+}. As a result, an increase in the amount of Mo in the experimental samples results in an augment in the value of ρ.

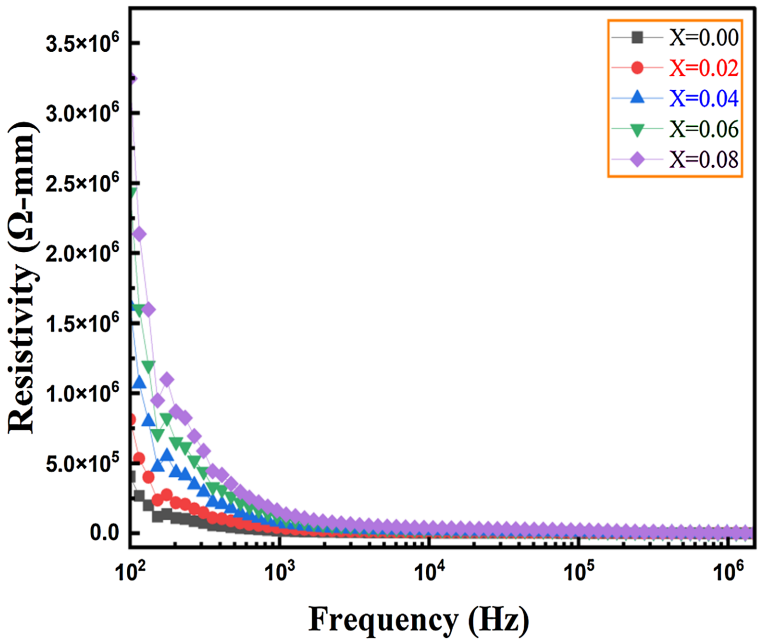

Figure 9. Variation of ρ with the frequency for different CSMMO ceramics.

3.8. AC Conductivity

Figure 10 shows the AC conductivity (σ_{ac}) behavior of CSMMO ceramics in response to the frequency. In order to have a better understanding of the electrode polarization effect, the measurements of σ_{ac} were performed. Figure 10 illustrates that the variation of σ_{ac} comprises three unique zones: The low-frequency

dispersive region I, the intermediate-frequency plateau region II, and the high-frequency dispersive zone III. The variation of σ_{ac} with frequency can be articulated according to Jonscher's power law.

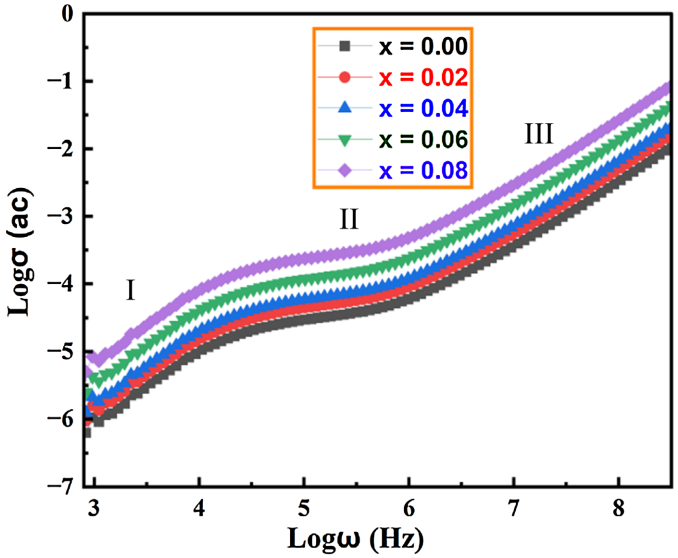

Figure 10. Variation of σ_{ac} with frequency for different CSMMO ceramics.

$$\sigma_{ac}(T) = \sigma_0(0) + A\omega^n \tag{17}$$

where $\sigma_{ac}(T)$ is the total conductivity, $\sigma(0)$ is the frequency-independent conductivity, *i.e.*, dc conductivity in the low-frequency region. The second term $A\omega^n$ is assigned to the high-frequency dispersive region, where the exponent n ($0 < n < 2$) corresponds to a localized or re-orientational short-range hopping motion within the grain. Thus, the conduction mechanism in the low-frequency dispersive zone (region-I) is attributed to long-range hopping linked to the grain boundaries [19], while in the high-frequency dispersive area (region-III), it is due to localized or re-orientational short-range hopping within the grain [39]. The minor plateau in the middle frequency band (region-II) may be ascribed to random hopping [40]. The conductivity exhibits a significant rise with frequency, indicating conduction resulting from the hopping of charge carriers between ions through an oxygen atom. The relationship between σ_{ac} *vs.* logω should be linear, as per Jonscher's power law. However, a divergence from the power law in the low-frequency band distinctly indicates the presence of an electrode polarisation effect across all compositions [28]. As shown in **Figure 10**, the σ_{ac} is found maximum at higher frequencies which might be attributed to the compound's thermal process because of the influence of charge carriers. The carriers of charge have sufficient time to build up at the sample-electrode surfaces in low-frequency settings, which leads to electrode polarization effects [12]. At low frequencies, conductivity is diminished due to the influence of active grain boundaries, resulting in a delay of mobile charge carriers [41]. The electrical properties of the prepared compound are studied here by observing resistivity and conductivity. The impact of Mo

doping was evident in the conductivity analyses, enhanced conduction (ac conductivity) due to the presence of charge carriers and the largest effect was observed at 8% Mo dopant content. Here the charge carriers which are responsible to make change in the conduction process arise from the two mechanisms, one from the exchange of $Mn^{3+} \leftrightarrow Mn^{4+}$ and other one is crystal defects caused by Mo-doping produce more dipoles in the ac field.

3.9. Permeability Study

The permeability is a measurement of a material's ability to strengthen the production of a magnetic field within itself. The most favourable magnetic properties of perovskite are to obtain high permeability with low loss at high frequency. The variation of the real part of initial permeability (μ_i') with composition is quite difficult to describe, because it depends on many factors, such as stoichiometry, grain size, impurity contents, coercive field, porosity etc. [42]. Therefore, the study of μ_i' has been a subject of great interest from both theoretical and practical points of view. **Figure 11(a)** represents the variation of the μ_i', as a function of frequency. It is evident that the value of μ_i' of all samples initially increases gradually up to 2400Hz and, then, remains frequency-independent. The frequency at which μ_i' reaches its highest value and then abruptly drops is referred to as resonance frequency (f_r). When the applied frequency and the natural frequency of the magnetic spins match, resonance happens [8]. The perovskites' compositional stability and region of appropriateness are contingent upon a broad range of frequencies, within which the value of μ_i' is observed to remain constant. The high-frequency stability of permeability renders the perovskite compatible with numerous high-frequency applications [43]. The value of μ_i' has been found to decrease with the substitution of 2% Mo content and then increase upto 6% Mo content, where it again decreases at 8% Mo content. The highest value of μ_i' has been found for 6% dopant. Two mechanisms could be resolved μ_i', such as the domain wall displacement and the spin rotation in the domains, *i.e.*, total domain spin. The permeability, resulting from the domain wall motion is followed the equations [15], $\mu_i' - 1 = \frac{3\pi M_s^2 D}{4\gamma}$, where, D represents the value of grain size, M_s^2 is the saturation magnetization and γ represents the domain wall energy. As shown of **Figure 4**, the size of grains is increased with the concentration of Mo and this may contribute to improve the value of μ_i'. The initial decrease in μ_i' suggests that the effect of stoichiometry play a dominant role at lower values of *x*. The mobility of the domain wall can be altered by the concentration of oxygen vacancies, which establishes a mechanical barrier to the domain wall [44]. On account of the fluctuation in the concentration of oxygen vacancies, the value of μ_i' fluctuates in accordance with the amount of Mo present. Related research showed that the fluctuations of the μ_i' may be caused by the size effect and the existence of the Mn-O bond [8]. The permeability is diminished because of decreasing grain size; however, the stability of permeability is increased due to

the influence of the domain wall motion by the small grain size [8] [43].

The frequency dependence of the magnetic loss tangent ($\tan\delta_M$) of the compositions is shown in **Figure 11(b)**. The loss occurs as a result of the domain walls beginning to lag behind in following the applied alternating field, which can be attributed to the flaws that are present in the lattice.

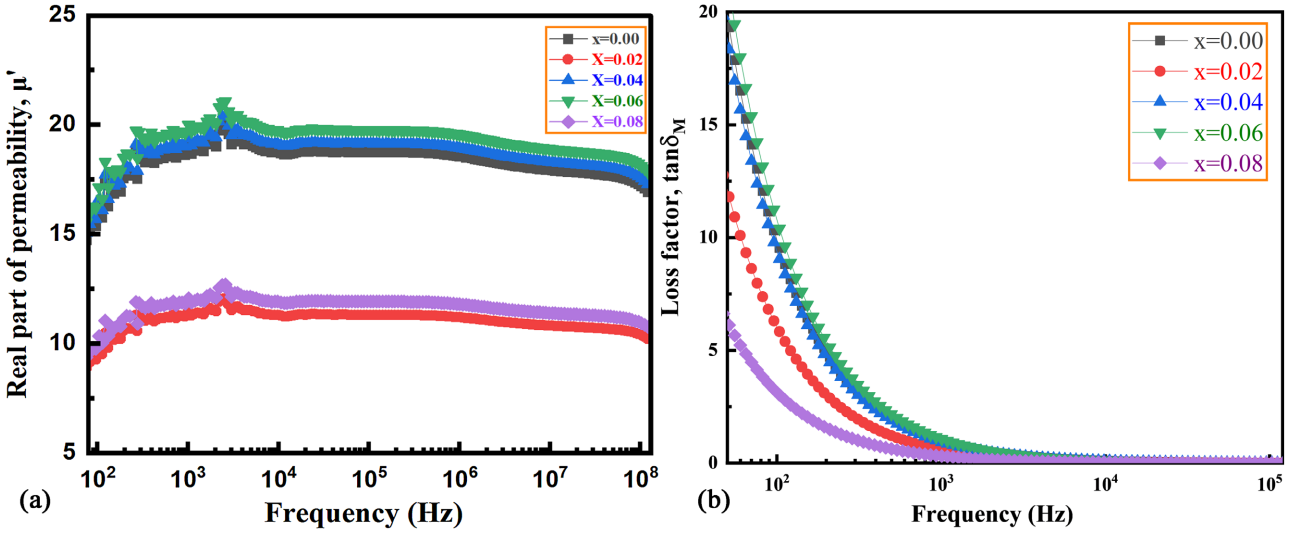

Figure 11. Frequency-dependent variation of (a) μ_i' and (b) $\tan\delta_M$ for various compositions of CSMMO ceramics.

It should be mentioned that $\tan\delta_M$ is susceptible to many views, such as the mobility of charge carriers, porosity, domain defects, the concentration of dipoles, hysteresis loss, eddy current loss, residual loss, etc. As observed from **Figure 11(b)**, the values of $\tan\delta_M$ for all samples initially decreased exponentially with the increase in the frequency (≤1000 Hz), and subsequently became almost constant up to 20 MHz. The drop in $\tan\delta_M$ with the increase in the frequency is caused, beyond some critical frequencies, because the domain wall motion cannot follow the applied electric field [7] [44]. The $\tan\delta_M$ can be observed to have a very small value at higher frequencies, which is one of the important requirements of the material to be used in microwave devices [45]. In the microwave frequency range, the magnetic loss of $CaMnO_3$ could almost be neglected. It implies that the microwave absorption property of $CaMnO_3$ is, usually, dependent on its magnetic loss [46]. The lowest $\tan\delta_M$ has been obtained for the samples $x \geq 0.06$. Smaller values of $\tan\delta_M$ are required for high-frequency magnetic applications [10]. Magnetic permeability is the ability of magnetic material to support magnetic field development. Higher the magnetic permeability, higher is the material's ability to produce field within it. In other words, it helps one to determine how much magnetic flux allows passing through a material. A material selected for a magnetic core in the electrical machine should have "high permeability" so that required magnetic flux can be produced in the core by fewer ampere-turns. So the studied the compound carrying high permeability may play an important role for high performance magnetic materials.

3.10. Study of DC Magnetization

The magnetization *vs.* magnetic field (M-H) hysteresis loops of CSMMO ceramics were taken at room temperature (300 K) and also at low temperature (5 K). Figure 12(a) shows the field-dependent magnetization curves of the studied compound at room temperature (300 K). The M-H hysteresis loops were carried out using a Physical Property Measurement System (PPMS). The paramagnetic behavior is noticed at room temperature for the undoped $Ca_{0.9}Sr_{0.1}MnO_3$ solid solution. The various parameters, like coercivity (H_c), magnetization (M), and retentivity (M_r), for all compositions have been calculated from the PPMS analysis, and the values are listed in Table 4. It can be observed that with the increase in Mo concentration, the decrease in the coercivity has occurred from 6% Mo content, and an increasing trend is exhibited for 2% to 4%. The M_r values increase up to 2% Mo content and, then, decrease. Enhanced M, with very small values, is seen, indicating an antiferromagnetic phase with weak ferromagnetism [17] for the prepared compositions. The reason for the observation of weak ferromagnetism in the Mo-doped ceramics may be attributed to the enhancement of oxygen vacancy in the sample and also the reduction of magnetic ions Mn^{3+} [47] [48].

Figure 12(b) shows the field-dependent magnetization curves of Mo-doped

Table 4. Magnetization, retentivity, and coercivity for CSMMO ceramics.

Content (x)	M (emu/g)		M_r (emu/g)		H_c (kOe)	
	300 K	5 K	300 K	5 K	300 K	5 K
0.00	0.716	1.554	0.0021	0.05613	0.03599	0.47057
0.02	0.77055	1.176054	0.00434	0.039761	0.109834	0.3499
0.04	0.03997	1.3298	0.03997	0.013752	0.04191	0.19507
0.06	0.8581	1.2457	0.0022	0.0012	0.024723	0.0178
0.08	0.8574	1.0468	0.00145	0.0011452	0.036799	0.02058

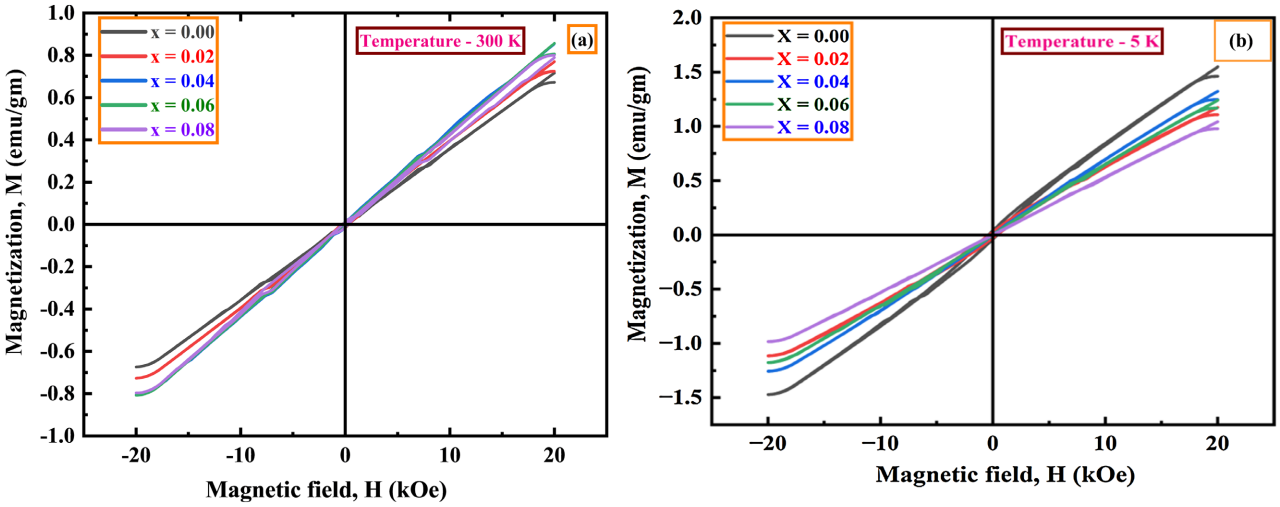

Figure 12. M-H hysteresis loops of CSMMO ceramics: (a) at room temperature (300 K) and (b) at low temperature (5 K).

CSMMO ceramics at low temperatures (5 K). The figure shows the M-H curves for ceramics with an applied magnetic field up to ±20,000 Oe. Up to $x = 0.02$ sample, small magnetic hysteresis has been observed. Parent composition $CaMnO_3$ shows antiferromagnetic behavior at low temperatures, while substitution of Mo at Mn site shows melting of antiferromagnetic state. The various calculated parameters (M, M_r, and H_c) are tabulated in **Table 4**. It can be observed that with increasing doping contents, M_r under goes a decrease. The value of M and the H_c also decreases linearly with dopant contents. But the values of M, M_r, and H_c are found to be larger at low temperatures than at room temperature. But complete saturation has not been observed even at 5 K, which reveals a superposition of both ferromagnetic and antiferromagnetic (AFM) components [15] [42]. With increasing the doping level of Mo, the M decreases due to the enhanced Mn^{3+}/Mn^{3+} AFM interaction. The magnetization originated due to the competition between AFM and paramagnetic (PM) states with the substitution of Mo at the Mn site in $CaMnO_3$. This behavior of magnetization of Mo-doped compositions is due to the structural transformation of the compositions [3]. The competition between AFM and PM states has been found in the compositions of $x = 0.02$, 0.04, and 0.08. Further, the change in space group for composition $x = 0.06$ and 0.08 results in the complete transformation of the AFM state into the PM state. The substitution of Mo for manganese (Mn) in the CSMMO showed AFM with a C-type orbital polarization or associated with ordered stripes, significantly increasing with dopant concentration of Mo [36]. Besides, the orthorhombic CSMMO compositions have a magnetic state with G-type order corresponding to the coupling between Mn and the first Mn-neighbors in an AFM type, while the second Mn-neighbors are in an FM type. The AFM ordering is mainly favorable by the mutual interaction between Mn^{4+}-Mn^{4+} cations *via* O^{2-} anion (*i.e.*, Mn^{4+}-O^{2-}-Mn^{4+}) [21]. It is also possible for CSMMO compositions, the G-type, and C-type AFM can result in orthorhombic to tetragonal structure, respectively, and the competition between correlations of a G-type AFM order and a C-type AFM order accompanying a $3d_{3z^2-r^2}$ orbital order, leading to the more complicated magnetic phase diagram [14].

4. Conclusion

The polycrystalline $Ca_{0.9}Sr_{0.1}Mn_{1-x}Mo_xO_3$ (CSMMO with $x = 0.00$, 0.02, 0.04, 0.06, and 0.08) solid solutions were synthesized following the standard solid-state reaction method and sintered at 1300˚C for 4 hours. The influence of Mn substitution by Mo in the crystal structure, microstructure, optical properties, electrical properties, complex initial permeability, and DC magnetization of the prepared compositions were carried out. The compound exhibited perovskite structure with the transformation of phase from orthorhombic symmetry for $x = 0.00$ to $x = 0.04$ samples into a tetragonal symmetry for the samples $x = 0.06$ and $x = 0.08$. The size of grains was determined from the FESEM images, and the values increased with the increase in Mo concentration. The optical properties of Mo-doped

$Ca_{0.9}Sr_{0.1}MnO_3$ ceramics were examined by the UV-vis spectral studies and the Fourier Transform Infrared Spectroscopy (FTIR). It was seen that the optical band gaps of CSMMO ceramics were indirect band gaps, and the values firstly decreased with doping content up to 2% and, then, increased for 4% to 6% Mo contents, where it again very slightly decreased for 8% Mo content. The electrical properties, such as resistivity and AC conductivity, were collected using the Impedance analyzer at room temperature. The resistivity as well as the AC conductivity increased with the addition of dopant concentration. The frequency-dependent conductivity spectra showed three distinct regions. The complex initial permeability (μ_i') of all samples exhibited a resonance around 2.4 kHz. The μ_i' was found to be enhanced with the addition of Mo and the highest value was noticed for the 6% Mo dopant sample. On the other hand, the lowest loss factor was obtained for the samples $x \geq 0.06$. The M-H hysteresis loops of various $Ca_{0.9}Sr_{0.1}Mn_{1-x}Mo_xO_3$ ceramics were measured both at room temperature (300 K) and low temperature (5 K) with an applied magnetic field up to ±20 kOe. The values of saturation magnetization (M_s) and retentivity (M_r) were found to be larger at low temperatures than at room temperature (RT), although no saturation was obtained for any compositions. A competition between antiferromagnetic and paramagnetic states was found with the substitution of Mo in the compound for $x = 0.02$, 0.04, and 0.08 samples, and this behavior of magnetization might be attributed to the structural transformation.

Acknowledgements

The authors sincerely appreciate the financial support provided by Comilla University, Cumilla, Bangladesh, for this research.

Conflicts of Interest

The authors declare no conflicts of interest regarding the publication of this paper.

References

[1] Saavedra Gaona, I.M., Caro Anzola, E.W., Turatti, A.M., Pimentel, J.L., Mesquita, F., Morán, O., *et al.* (2021) Effects of Tm-Doping on Structural, Magnetic and Transport Properties in $CaTi_{0.8}TM_{0.2}O_3$ (TM = Mo, Co, and Mn). *Ceramics International*, **47**, 9984-9989. https://doi.org/10.1016/j.ceramint.2020.12.144

[2] Yin, Y. and Li, Q. (2017) A Review on All-Perovskite Multiferroic Tunnel Junctions. *Journal of Materiomics*, **3**, 245-254. https://doi.org/10.1016/j.jmat.2017.09.001

[3] Loshkareva, N.N. and Mostovshchikova, E.V. (2012) Electron-Doped Manganites Based on $CaMnO_3$. *The Physics of Metals and Metallography*, **113**, 19-38. https://doi.org/10.1134/s0031918x12010073

[4] Zhang, F.P., Lu, Q.M., Zhang, X. and Zhang, J.X. (2011) First Principle Investigation of Electronic Structure of $CaMnO_3$ Thermoelectric Compound Oxide. *Journal of Alloys and Compounds*, **509**, 542-545. https://doi.org/10.1016/j.jallcom.2010.09.102

[5] Freeland, J.W., Chakhalian, J., Boris, A.V., Tonnerre, J.-J., Kavich, J.J., Yordanov, P., *et al.* (2010) Charge Transport and Magnetization Profile at the Interface between the Correlated Metal $CaRuO_3$ and the Antiferromagnetic Insulator $CaMnO_3$. *Physical*

Review B, **81**, Article 094414. https://doi.org/10.1103/physrevb.81.094414

[6] Benedek, N.A., Mulder, A.T. and Fennie, C.J. (2012) Polar Octahedral Rotations: A Path to New Multifunctional Materials. *Journal of Solid State Chemistry*, **195**, 11-20. https://doi.org/10.1016/j.jssc.2012.04.012

[7] Supelano, G.I., Barón-González, A.J., Martinez Buitrago, D., Santos, A.S., Parra Vargas, C.A., Corredor, L.T., *et al.* (2014) Structural and Magnetic Study of $CaMn_{1-X}Mo_XO_3$ (x = 0.08, 0.10, 0.12) System. *Journal of Superconductivity and Novel Magnetism*, **28**, 259-264. https://doi.org/10.1007/s10948-014-2855-y

[8] Liu, Y., Zhu, D., Qing, Y. and Luo, F. (2021) Study on Effect of Doping Content on the Microstructure, Dielectric and Microwave Absorption Properties of X-NiO/$CaMn_{1-X}O_3$. *Journal of Materials Science*: *Materials in Electronics*, **32**, 14874-14884. https://doi.org/10.1007/s10854-021-06040-z

[9] Jiang, F., Zheng, J., Liang, L., Zhang, M. and Wang, Y. (2015) Microwave Absorbing Properties of $La_{0.1}Ca_{0.9}MnO_3$ Porous Microsphere Synthesized by Method of Precipitation. *Journal of Materials Science*: *Materials in Electronics*, **26**, 2243-2247. https://doi.org/10.1007/s10854-015-2676-1

[10] Liu, Y., Zhu, D., Chai, X., Qing, Y. and Zhou, W. (2021) Enhanced Dielectric and Microwave Absorption Properties of $CaMnO_3$ Powders by Sr Doping in the 8.2 - 18 GHZ Band. *Ceramics International*, **47**, 13339-13343. https://doi.org/10.1016/j.ceramint.2021.01.190

[11] Wahba, O.A.G., Hassan, A.M., El-Wahab, H.A., Mohy-Eldin, A., Naser, A.M. and Fouad, O.A. (2015) Synthesis of Nanosized Mixed Metal Oxides Heat and Corrosion Resistant Pigments: $CaMnO_3$, $Ca_2Cr_2O_5$ and $CaSb_2O_6$. *Pigment & Resin Technology*, **44**, 379-385. https://doi.org/10.1108/prt-06-2014-0049

[12] Taguchi, H., Kugi, T., Kato, M. and Hirota, K. (2010) Fabrication of (Ca_1-XLAX) MnO_3 Ceramics with a High Relative Density and Their Power Factor. *Journal of the American Ceramic Society*, **93**, 3009-3011. https://doi.org/10.1111/j.1551-2916.2010.03987.x

[13] Leonidov, I.A., Konstantinova, E.I., Patrakeev, M.V., Chukin, A.V. and Kozhevnikov, V.L. (2017) Electron Transport and Mobility Analysis in La/Sr Co-Doped $CaMnO_{3-\delta}$. *Journal of Solid State Electrochemistry*, **21**, 2099-2108. https://doi.org/10.1007/s10008-017-3571-x

[14] Okuda, T. and Fujii, Y. (2010) Cosubstitution Effect on the Magnetic, Transport, and Thermoelectric Properties of the Electron-Doped Perovskite Manganite $CaMnO_3$. *Journal of Applied Physics*, **108**, Article 103702. https://doi.org/10.1063/1.3505756

[15] Neetika Das, A., Dhiman, I., Nigam, A.K., Yadav, A.K., Bhattacharyya, D., *et al.* (2012) Transport and Magnetic Properties of Fe Doped $CaMnO_3$. *Journal of Applied Physics*, **112**, Article 123913. https://doi.org/10.1063/1.4770378

[16] Kumar, S., Ram, I., Kumar, A. and Kumar, U. (2020) Structural, Optical, and Low-Temperature Resistivity of Ca-Doped $PrMnO_3$ Nanoparticles. *Emergent Materials*, **3**, 595-604. https://doi.org/10.1007/s42247-020-00125-x

[17] Nandan, K.R. and Kumar, A.R. (2016) Electrical Properties of $Ca_{0.925}Ce_{0.075}Mn_{1-X}Fe_XO_3$ (x = 0.1 - 0.3) Prepared by Sol-Gel Technique. *Journal of Materials Science*: *Materials in Electronics*, **27**, 13179-13191. https://doi.org/10.1007/s10854-016-5464-7

[18] Suzuki, T., Sakai, H., Taguchi, Y. and Tokura, Y. (2011) Thermoelectric Properties of Electron-Doped $SrMnO_3$ Single Crystals with Perovskite Structure. *Journal of Electronic Materials*, **41**, 1559-1563. https://doi.org/10.1007/s11664-011-1860-1

[19] Zhang, F.P., Zhang, X., Lu, Q.M., Zhang, J.X. and Liu, Y.Q. (2011) Electronic

Structure and Thermal Properties of Doped $CaMnO_3$ Systems. *Journal of Alloys and Compounds*, **509**, 4171-4175. https://doi.org/10.1016/j.jallcom.2011.01.032

[20] Srivastava, D., Azough, F., Freer, R., Combe, E., Funahashi, R., Kepaptsoglou, D.M., *et al.* (2015) Crystal Structure and Thermoelectric Properties of Sr-Mo Substituted $CaMnO_3$: A Combined Experimental and Computational Study. *Journal of Materials Chemistry C*, **3**, 12245-12259. https://doi.org/10.1039/c5tc02318a

[21] Lamhani, M., Chchiyai, Z., Elomrani, A., Manoun, B. and Hasnaoui, A. (2022) The Effect of Sr Substitution on the Structural and Physical Properties of Manganite Perovskites $Ca_{1-X}Sr_XMnO_{3-\delta}$ ($0 \leq x \leq 1$). *Physical Chemistry Chemical Physics*, **24**, 19414-19431. https://doi.org/10.1039/d2cp01096h

[22] Žužić, A., Filipan, V., Sutlović, I. and Macan, J. (2022) Perovskite Oxides for Energy Applications. *Tehnički Vjesnik*, **29**, 1419-1425. https://doi.org/10.17559/TV-20210716122507

[23] Liu, K.K., Liu, Z.Y., Zhang, F.P., Zhang, J.X., Yang, X.Y., Zhang, J.W., *et al.* (2019) Improved Thermoelectric Performance in Pr and Sr Co-Doped $CaMnO_3$ Materials. *Journal of Alloys and Compounds*, **808**, Article 151476. https://doi.org/10.1016/j.jallcom.2019.07.188

[24] Nurhaziqah, A.M.S., Afiqah, I.Q., Hisam Abd. Aziz, M.F., Aziz, N.A.N., Zalani Daud, M., Hasiah, S., *et al.* (2020) Microstructure Study of Calcium Manganese Oxide ($CaMnO_3$) as Perovskite Materials. *Journal of Physics: Conference Series*, **1535**, Article 012024. https://doi.org/10.1088/1742-6596/1535/1/012024

[25] Hayashi, H. (1999) Structural Consideration on the Ionic Conductivity of Perovskite-Type Oxides. *Solid State Ionics*, **122**, 1-15. https://doi.org/10.1016/s0167-2738(99)00066-1

[26] Souza, A.D., Babu, P.D., Rayaprol, S., Murari, M.S. and Daivajna, M. (2020) Study of Combined Effect of Partial Bi Doping and Particle Size Reduction on Magnetism of $La_{0.7}Sr_{0.3}MnO_3$. *Journal of Magnetism and Magnetic Materials*, **497**, Article 166020. https://doi.org/10.1016/j.jmmm.2019.166020

[27] Souza, A.D., Vagadia, M. and Daivajna, M.D. (2021) Finite-Size Effects on the Evolution of Magnetic Correlations and Magnetocaloric Properties of $Pr_{0.4}Bi_{0.2}Sr_{0.4}MnO_3$. *Applied Physics A*, **127**, Article No. 677. https://doi.org/10.1007/s00339-021-04828-8

[28] Yudanto, S.D., Ari Adi, W. and Imaduddin, A. (2018) Characterization and Studies on AC Conductivity of $CaMnO_3$ Material. *Journal of Physics: Conference Series*, **1091**, Article 012023. https://doi.org/10.1088/1742-6596/1091/1/012023

[29] Dixit, G., Kumar, P., Negi, P. and Asokan, K. (2017) Investigations of Structural and Transport Properties of Ca Doped Yttrium Manganites. *Ferroelectrics*, **516**, 74-81. https://doi.org/10.1080/00150193.2017.1362286

[30] Alcock, C.B., Kubaschewski, O. and Spencer, P.J. (1993) Materials Thermochemistry. Pergamon Press.

[31] Portia, S.A.U., Srinivasan, R., Elaiyappillai, E., Johnson, P.M. and Ramamoorthy, K. (2020) Facile Synthesis of Eu-Doped $CaTiO_3$ and Their Enhanced Supercapacitive Performance. *Ionics*, **26**, 3543-3554. https://doi.org/10.1007/s11581-020-03494-9

[32] Lucio, B., Romero, M. and González-Aguilar, J. (2019) Analysis of Solid-State Reaction in the Performance of Doped Calcium Manganites for Thermal Storage. *Solid State Ionics*, **338**, 47-57. https://doi.org/10.1016/j.ssi.2019.05.007

[33] Mostovshchikova, E.V., Naumov, S.V., Makhnev, A.A., Solin, N.I. and Telegin, S.V. (2014) Evolution of the Optical Properties and the Electrical Resistivity of $CaMnO_3$ during the Substitution of Mo for Mn Ions. *Journal of Experimental and Theoretical*

Physics, **118**, 297-303. https://doi.org/10.1134/s1063776114010257

[34] Melo Jorge, M.E., Correia dos Santos, A. and Nunes, M.R. (2001) Effects of Synthesis Method on Stoichiometry, Structure and Electrical Conductivity of $CaMnO_{3-\delta}$. *International Journal of Inorganic Materials*, **3**, 915-921. https://doi.org/10.1016/s1466-6049(01)00088-5

[35] Mastronardo, E., Qian, X., Coronado, J.M. and Haile, S. (2019) Fe-Doped $CaMnO_3$ for Thermochemical Heat Storage Application. *AIP Conference Proceedings*, Casablanca, 2-5 October 2018, Article 210005. https://doi.org/10.1063/1.5117754

[36] Martin, C., Maignan, A., Hervieu, M., Raveau, B. and Hejtmanek, J. (2001) Electron Doping in $CaMnO_3$ Induced by Mo for Mn Substitution: An Efficient Route to Orbital and Charge Ordering. *Physical Review B*, **63**, Article 100406. https://doi.org/10.1103/physrevb.63.100406

[37] Sotelo, A., Depriester, M., Torres, M.A., Sahraoui, A.H., Madre, M.A. and Diez, J.C. (2018) Effect of Simultaneous K, and Yb Substitution for Ca on the Microstructural and Thermoelectric Characteristics of $CaMnO_3$ Ceramics. *Ceramics International*, **44**, 12697-12701. https://doi.org/10.1016/j.ceramint.2018.04.071

[38] Zhang, F.P., Zhang, X., Lu, Q.M., Zhang, J.X., Liu, Y.Q., Fan, R.F., *et al.* (2011) Doping Induced Electronic Structure and Estimated Thermoelectric Properties of $CaMnO_3$ System. *Physica B*: *Condensed Matter*, **406**, 1258-1262. https://doi.org/10.1016/j.physb.2011.01.011

[39] Sen, A., Hasan, M.K., Islam, Z., Hassan, M.R.A., Zaman, T., Matin, M.A., *et al.* (2020) Influence of Ba and Mo Co-Doping on the Structural, Electrical, Magnetic and Optical Properties of $BiFeO_3$ Ceramics. *Materials Research Express*, **7**, Article 016312. https://doi.org/10.1088/2053-1591/ab6801

[40] Science, A.C. and Materials, E. (2013) Physicochemical Properties of the $Sr_{1-x}Ca_x RuO_3$ ($0 \le x \le 1.0$). *Physical Review B* (Condensed Matter), **56**, 321-329. https://doi.org/10.1103/PhysRevB.56.321

[41] Atta, N.F., Galal, A. and El-Ads, E.H. (2016) Perovskite Nanomaterials—Synthesis, Characterization, and Applications. In Tech. https://doi.org/10.5772/61280

[42] Kompany, A., Ghorbani-Moghadam, T., Kafash, S. and Ebrahimizadeh Abrishami, M. (2014) Frequency Dependence of Néel Temperature in $CaMnO_{3-\delta}$ Ceramics: Synthesized by Two Different Methods. *Journal of Magnetism and Magnetic Materials*, **349**, 135-139. https://doi.org/10.1016/j.jmmm.2013.08.015

[43] Zhao, S., Zheng, J., Jiang, F., Song, Y., Sun, M. and Song, X. (2015) Co-Precipitation Synthesis and Microwave Absorption Properties of $CaMnO_3$ Doped by La and Co. *Journal of Materials Science*: *Materials in Electronics*, **26**, 8603-8608. https://doi.org/10.1007/s10854-015-3534-x

[44] Xu, G. (2004) High-Temperature Transport Properties of Nb and Ta Substituted $CaMnO_3$ System. *Solid State Ionics*, **171**, 147-151. https://doi.org/10.1016/s0167-2738(03)00108-5

[45] Shishkin, A., Koppel, T., Mironov, V., Hussainova, I., Locs, J. and Haldre, H. (2017) Microwave Reflectance and Transmittance Properties of Conductive Composite Materials. *Energy Procedia*, **113**, 354-361. https://doi.org/10.1016/j.egypro.2017.04.006

[46] Nurhayati, A., Venkataramana, K., Modem, N. and Reddy, C.V. (2021) Effects of Different Sintering Methods on the Structural and Electrical Properties of $Ca_{0.9}Sr_{0.1}MnO_3$. *Ceramics International*, **47**, 26822-26828. https://doi.org/10.1016/j.ceramint.2021.06.090

[47] Singh, B. and Manoharan, S.S. (2011) Structural Transformation and Magnetic Properties of $CaMn_{1-x}Fe_xO_{3-\delta}$ ($0.0 \leq x \leq 0.5$). *Materials Letters*, **65**, 2029-2031. https://doi.org/10.1016/j.matlet.2011.04.025

[48] Lu, W.J., Sun, Y.P., Ang, R., Zhu, X.B. and Song, W.H. (2007) Effect of Mo Substitution in the n = 3 Ruddlesden-Popper Compound $Ca_4Mn_3O_{10}$. *Physical Review B*, **75**, 1-7.